Energy Loss Analysis of Two-Terminal Tandem PV Systems under Realistic Operating Conditions—Revealing the Importance of Fill Factor Gains

Blom, Youri; Vogt, Malte Ruben; Ruiz Tobon, Carlos M. ; Santbergen, Rudi; Zeman, Miro; Isabella, Olindo

Important note
To cite this publication, please use the final published version (if applicable).
Please check the document version above.

Energy Loss Analysis of Two-Terminal Tandem PV Systems under Realistic Operating Conditions—Revealing the Importance of Fill Factor Gains

Youri Blom,* Malte Ruben Vogt,* Carlos M. Ruiz Tobon, Rudi Santbergen, Miro Zeman, and Olindo Isabella

The tandem PV technology can potentially increase the efficiency of PV modules over 30%. To design efficient modules, a quantification of the different losses is important. Herein, a model for quantifying the energy loss mechanisms in PV systems under real-world operating conditions with a level of detail back to the components and their fundamental properties is presented. Totally, 17 losses are defined and divided into four categories (fundamental, optical, electrical, and system losses). As example, a system based on $a > 29\%$ two-terminal perovskite/silicon tandem cell is considered. The loss distribution at standard test conditions is compared to four geographical locations. The results show that the thermalization, reflection, and inverter losses increase by 1.2%, 1.1%, and 1.4%, respectively, when operating outdoors. Additionally, it is quantified how fill factor gains partly compensate the current mismatch losses. For example, a mismatch of 7.0% in photocurrent leads to a power mismatch of 1.2%. Therefore, the power mismatch should be used as indicator for mismatch losses instead of a current mismatch. Finally, herein, it is shown that solar tracking increases not only the in-plane irradiance but also the efficiency of the tandem module.

1. Introduction

To design efficient PV systems, it is important to have an overview of the different loss mechanisms and the ability to quantify them.[1,2] Moreover, research in the energy loss analysis has resulted in important insights for PV technology.[3]

This work presents a model for quantifying the different loss mechanisms in a PV system with perovskite/crystalline silicon

PV modules with a level of detail back to the properties at cell level. Similar studies have already calculated the loss analysis for crystalline solar cells.[1,3–8] However, no literature has been found on a complete energy loss analysis with a quantification of different loss mechanisms for a tandem cell. Also, the loss analysis is typically done at cell level, whereas our model includes losses at module and system level. Furthermore, this study also includes the energy loss analysis under outdoors conditions, which are typically different to standard test conditions.[9] Finally, solar tracking is implemented to study its effects on the loss distribution. In this study, horizontal (azimuth), vertical (altitude), and full tracking is simulated for the different locations.

2. Experimental Section

This work is an extension of the PVMD Toolbox.[10] The PVMD Toolbox can simulate the energy yield of a PV system based on their fundamental material properties and first-principle physics. First, a brief overview of the Toolbox is given, followed by a detailed explanation of the energy loss analysis model.

2.1. The PVMD Toolbox

The PVMD Toolbox consists of seven models that each simulate a different aspect of the PV system. The models are simulated sequentially, and each model uses the simulated data from the previous models. These models range from simulations at cell level to simulations at module level. A detailed description of all models can be found in the work of Vogt et al.[10]

The first model is the optical model, which calculates the reflectance, transmittance, and the absorption in each layer. This is followed by the semiconductor model, which provides the electrical characteristics of different cells. After this, two models (the mounting condition model and the irradiance model) calculate the absorbed irradiance at each moment in time. A thermal model is then used to calculate the temperature of each cell. The last two models are electrical models that provide the electrical parameters of each module (fill factor,

Y. Blom, M. R. Vogt, C. M. Ruiz Tobon, R. Santbergen, M. Zeman, O. Isabella
Photovoltaic Materials and Devices group
Delft University of Technology
Mekelweg 4, 2628CD Delft, The Netherlands
E-mail: Y.Blom@tudelft.nl; M.Vogt@tudelft.nl

the maximum power point voltage and current, and the output power) and the total AC energy yield.

For standard test conditions (STC), the AM1.5 spectrum is simulated at a normal angle of the solar cell. For outdoors conditions, the DC yield is simulated for every hour of the year individually. The air mass is calculated with the SMARTS spectral irradiance model,[11] and the irradiance from each sky element is calculated with the Perez weather model.[12] The in-plane irradiance on the module is then calculated with the Monte–Carlo ray tracing software LUX[10] that can include for shading and albedo reflections. The solar cell temperature is modeled by using the fluid dynamic model.[10,13]

2.2. The Loss Analysis Model

We extend the current version of the Toolbox with an energy loss analysis model for PV systems. In this model, 17 different loss mechanisms are defined such that the sum of all the losses and the AC electricity equal the incoming in-plane irradiance. The 17 losses are divided over 4 different categories, as shown in **Figure 1**. The losses are calculated per category from left to right, starting with the fundamental losses. In the rest of this section, the equations for every loss mechanism are defined and the limitations of the model are discussed.

2.2.1. The Fundamental Losses

We consider fundamental losses as all losses considered for the Shockley–Queisser (SQ) limit.[14] The equations of these fundamental losses are mostly derived from the work of Hirst et al.[15] The considered fundamental losses are the thermalization, below bandgap, emission, Carnot, and angle mismatch losses. For the fundamental losses, the bandgap energies of perovskite (1.68 eV) and silicon (1.12 eV) are used. Furthermore, an ideal solar cell is considered, meaning it has a perfect external quantum efficiency (EQE) and no nonradiative recombination. A perfect EQE is defined as having a value of 1 up to the wavelength corresponding with the bandgap energy.

The thermalization loss of a single photon is the difference between its energy and the bandgap energy of the solar cell,[4] which will be dissipated as heat. The total thermalization losses (P_{term}) can then be calculated with an integral over all

wavelengths, as shown in Equation (1). The integral should be taken from over all wavelengths smaller than the wavelength corresponding to the bandgap energy (λ_g), which is written as

$$P_{term} = A_{mod} \cdot \int_0^{\lambda_g} \phi_{in}(\lambda) \left(\frac{h \cdot c}{\lambda} - E_g \right) d\lambda \tag{1}$$

where A_{mod} is the area of the module, $\phi_{in}(\lambda)$ is the photon flux for a given wavelength, h and c are Plank's constants and the speed of light, respectively, and E_g is the bandgap energy.

The below bandgap losses are accounting for all photons that cannot be absorbed due to insufficient energy.[4] This loss can be calculated by integrating over all wavelengths larger than λ_g, which is written as

$$P_{below} = A_{mod} \cdot \int_{\lambda_g}^{\infty} I_{in}(\lambda) d\lambda \tag{2}$$

where $I_{in}(\lambda)$ is the incoming irradiance for a given wavelength.

Like the sun, a solar cell also emits black body radiation. These emitted photons are lost and are considered as radiative recombination. The emission can be modeled with the generalized Plank equation[4,15,16]

$$\phi_{em}(\lambda, T, \mu, \Omega) = \frac{2 \cdot \Omega \cdot c}{\lambda^4} \cdot \frac{1}{e^{\frac{E-\mu}{kT-1}}} \tag{3}$$

where ϕ_{em} is the emitted photon flux, T is the temperature, μ is the chemical potential of the solar cell, and Ω is the solid angle. Because each emitted photon accounts for a loss equal to the bandgap energy, the emission losses can be written as

$$P_{emission} = A_{mod} \cdot \int_0^{\lambda_g} E_g \cdot \phi_{em}(\lambda, T_{cell}, q \cdot V_{opt}, \Omega) d\lambda \tag{4}$$

where T_{cell} is the temperature of the cell calculated with the fluid dynamic model, q is the charge of an electron, and V_{opt} is the optimal voltage that maximizes the power for an ideal solar cell.[15] Ω is the solid state of emission, which is 2π for monofacial cells and 4π for bifacial cells.[17–19]

The optimal voltage discussed before is lower than $\frac{E_g}{q}$. This voltage difference can be divided in the Carnot voltage loss (V_{Carnot}) and the angle mismatch voltage loss (V_{angle}). The Carnot loss (P_{Carnot}) and the angle mismatch loss (P_{angle}) can be calculated with

$$P_{carnot} = V_{carnot} \cdot I_{max} \tag{5}$$

$$P_{angle} = V_{angle} \cdot I_{max} \tag{6}$$

where I_{max} is the maximum output current, and it is the difference between the incoming photon flux and the emitted photon flux. A quantification of the fundamental losses of an ideal solar cell under AM1.5g spectrum is shown in **Figure 2**. Note that the presented upper limits differ from the SQ-limit[14] and the limit calculated by De Vos,[20] since the AM1.5G spectrum is considered instead of the plank spectrum. Our quantification of the fundamental losses under black body radiation match Shockley–Queisser and De Vos, the results are shown in the Supporting Information.
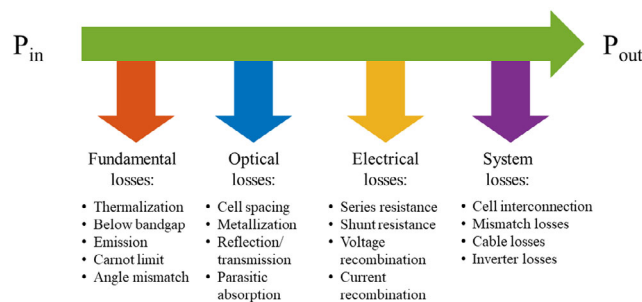
Figure 1. The 17 different losses that are considered. The losses are calculated from left to right.
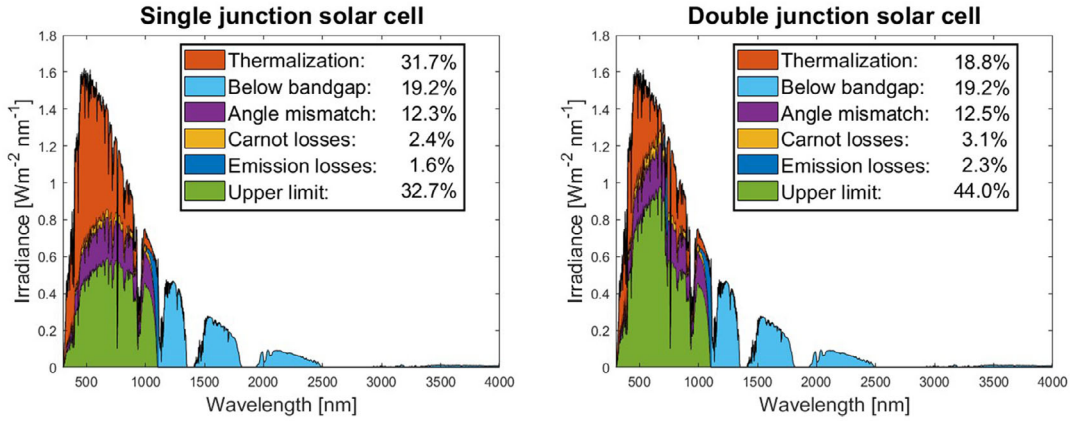
Figure 2. The fundamental losses and upper limit of a single junction Si (1.12 eV) solar cell and double junction perovskite (1.68 eV)/Si (1.12 eV) solar cell.

In addition to the five fundamental losses, a term called "nonideality effect" is added to account for a nonideal solar cell not matching the assumption used earlier. This includes that the emission losses are overestimated because the actual output voltage is typically smaller than the optimal voltage. It also accounts for absorption of photons with lower energy than the bandgap energy, as described by Urbach's rule.[21,22] Lastly, it accounts for an underestimation of the thermalization losses, which is only included for tandem modules. A more detailed description of the nonideality effect can be found in the supporting information.

2.2.2. The Optical Losses

The optical losses account for all photons (with a higher energy than the bandgap energy) that are not absorbed by the absorber material. The optical losses include cell spacing, metal shading, reflection/transmission, and parasitic absorption losses.

Both the cell spacing losses ($P_{cell-spacing}$) and metal shading losses (P_{metal}) can be considered as nonactive area losses. The cell spacing losses occur, since the areas of the solar cell do not completely fill the module area, and it can be calculated as

$$P_{cell-spacing} = (P_{in} - P_{fund}) \cdot \left(1 - \frac{N_{cells} \cdot A_{cell}}{A_{mod}}\right) \quad (7)$$

where P_{in} is the total incoming power, P_{fund} is the sum of the fundamental losses, N_{cells} is the number of cells, and A_{cell} is the area of a single cell.

The metal shading losses are calculated in a similar way as

$$P_{metal} = (P_{in} - P_{fund}) \cdot \frac{N_{cells} \cdot A_{cell}}{A_{mod}} \cdot SF \quad (8)$$

where SF is the shading factor that indicates what fraction of the solar cells is effectively covered by metal contacts.

The losses due to reflection and transmission ($P_{ref,trans}$) are calculated based on the results of the optical model of the Toolbox, since this provides the reflectance and transmittance of every wavelength. It can be calculated with

$$P_{ref,trans} = A_{eff} \cdot \int_0^{\lambda_g} (\phi_{in}(\lambda) - \phi_{em}(\lambda)) \cdot (R(\lambda) + T(\lambda)) \cdot q \cdot V_{opt} d\lambda \quad (9)$$

where A_{eff} is the effective area of the module, defined as the total cell area minus the nonactive area. $R(\lambda)$ and $T(\lambda)$ are, respectively, the reflection and transmittance for a certain wavelength. The term $q \cdot V_{opt}$ is used instead of the bandgap energy because the Carnot and angle mismatch voltage are already subtracted from these photons.

The parasitic absorption losses ($P_{par,abs}$) account for absorption by all materials in the module except for the cell absorbers, e.g., silicon and perovskite. The reflectance and transmittance in Equation (9) are replaced with the parasitic absorptance (α_{par}), written as

$$P_{par,abs} = A_{eff} \cdot \int_0^{\lambda_g} (\phi_{in}(\lambda) - \phi_{em}(\lambda)) \cdot \alpha_{par}(\lambda) \cdot q \cdot V_{opt} d\lambda \quad (10)$$

where the parasitic absorptance can be written as

$$\alpha_{par} = 1 - R(\lambda) - T(\lambda) - A_{Si}(\lambda) - A_{pvk}(\lambda) \quad (11)$$

where $A_{si}(\lambda)$ and $A_{pvk}(\lambda)$ are the absorption in the silicon and perovskite layers, respectively.

2.2.3. The Electrical Losses

After the optical losses, the electrical losses are calculated, which consist of resistive losses and recombination losses. The electrical characterization of the top and bottom cells is done using our advanced semiconductor analysis (ASA) software.[23] IV curves of top and bottom cells are simulated for various operating conditions (i.e., different temperatures (−15–95 °C) and different irradiances (50–1500 W m^{-2}) such that all real-world conditions are included by solving the Poisson equation and continuity equations in one dimension. To accelerate the computation, a one-diode equivalent circuit model[4,24–26] of the solar cell is fitted to match all the IV curves accurately.[10] This provides a calibrated lumped-element model (CLEM) with temperature- and illumination-dependent parameters.[10] The parameters included

in this model are the photogenerated current (I_{ph}), the diode ideality factor (n), saturation current (I_0), series resistance (R_s), and shunt resistance (R_{sh}). The temperature and irradiance dependencies of all the parameters can be found in the supporting information. IV-curves of the top and bottom cells are combined to obtain the IV curve of the tandem cell by creating a series connection. The electrical losses are calculated based on the temperature- and irradiance-dependent values of the five parameters.

The series resistance losses (P_{series}) and the shunt resistance losses (P_{shunt}) are, respectively, calculated with the following equations

$$P_{series} = I_{mpp}^2 \cdot R_s \tag{12}$$

$$P_{shunt} = \frac{(V_{mpp} + I_{mpp} \cdot R_s)^2}{R_{sh}} \tag{13}$$

In these equations, V_{mpp} is the maximum power point voltage, and I_{mpp} is the maximum power point current.

Besides radiative recombination, it is possible for electrons and holes to recombine without emitting a photon. This is known as nonradiative recombination.[4,7] This nonradiative recombination results in a voltage loss (V_{NRRV}) and a current loss (I_{NRRV}). The voltage loss is the difference between the optimal voltage and the voltage over the current source in the five-parameter model. The nonradiative recombination voltage loss (P_{NRRV}) can be written as

$$P_{NRRV} = (V_{opt} - V_{mpp} - V_{series}) \cdot I_{ph} \tag{14}$$

where V_{series} is the voltage over the series resistance.

The current loss can be modeled as the current flowing into the diode. The nonradiative recombination current loss (P_{NRRI}) can be calculated as

$$P_{NRRI} = (I_{ph} - I_{mpp} - I_{shunt}) \cdot (V_{mpp} + V_{series}) \tag{15}$$

where I_{shunt} is the current flowing into the shunt resistance.

2.2.4. The System Losses

The last category is the system losses. The considered losses are the interconnection, mismatch, cable, and inverter losses. The interconnection losses (P_{int}) occur since the interconnection between the cells typically has some resistance. The ohmic losses of the interconnection can be written as

$$P_{int} = I_{mod}^2 \cdot R_{int} \tag{16}$$

where I_{mod} is the output current of the module, and R_{int} is the resistance of the interconnection.

Mismatch losses are caused by differences in the maximum power point conditions among the cells. Because the cells are coupled, the operating conditions of an individual cell might differ from its maximum power point conditions. The mismatch losses (P_{mism}) are calculated as the difference between the sum of the individual maximum power points and the actual output power

$$P_{mism} = \sum_{i=1}^{N_{cells}} (P_{mpp,i}) - I_{mod} \cdot (V_{mod} + I_{mod} \cdot R_{int}) \tag{17}$$

In this equation, P_{mpp} is the maximum power point power of an individual cell i, and V_{mod} is the voltage of the module. The voltage over the interconnection has to be added to the module voltage, since this is the voltage over all the cells. Mismatch losses are especially important for two-terminal tandem modules, since the top and bottom cells need to be current matched.

When the DC electricity is converted into AC electricity, cables are installed, which typically introduce losses. The cable losses (P_{cable}) are calculated as

$$P_{cable} = P_{in,cable} \cdot (1 - \eta_{cable}) \tag{18}$$

where $P_{in,cable}$ is the electricity flowing into the cables, and η_{cable} is the efficiency of the cables that is provided by the inverter model of the Toolbox.

The last considered loss is the inverter loss. The inverter losses ($P_{inverter}$) are calculated by taking the differences between the incoming electricity (P_{DC-in}) and the final AC electricity (P_{AC}), written as

$$P_{inverter} = P_{DC-in} - P_{AC} \tag{19}$$

2.3. Validation of the Model

For every model, validation is an important aspect. The first type of validation is performed by comparing the fundamental losses with upper limits from literature, as the upper limit can be obtained by removing the fundamental losses. In the supporting information, it can be seen that the upper limits of the single junction and double junction solar cell are 30.0% and 42.0%. These values match the well-known upper limits from literature.[14,20]

Additionally, the PVMD Toolbox has been validated in a previous study.[10] In this study, it was shown that the simulated performance of c-Si modules nearly always falls within the 95% confidence interval. To analyze the effect of uncertainty in the input on the loss distribution, a sensitivity analysis is performed for the simulation of Amsterdam, which is shown in the supporting information. This shows that an uncertainty of 10% of the input (which is larger than the actual uncertainty), there is only an uncertainty of 0.1% in the loss distributions.

2.4. The Limitations of the Model

The described model includes several assumptions. First, the model assumes that there is no temperature dependence on the bandgap energies, when calculating the fundamental losses. In reality, however, the bandgap energy for both perovskite and silicon is dependent on the temperature.[27,28] For the electrical simulation, a temperature dependency is included for the bandgap energy.

Another effect that is not included in the model is photon recycling. In photon recycling, photons emitted by the top cell could be absorbed by the bottom cell,[29] reducing the emission losses.

This is not included in the model, as it would be challenging to implement with the workflow of the PVMD Toolbox as it would require an iterative process of optical and electrical simulations. Moreover, the emission losses, which would potentially trigger this process, are below 3% in all simulations.

Finally, it should be noted that the five-parameter model does not include effects such as hysteresis or the double diode effect. The former would require that the system knows its previous steps on the hysteresis curve and additionally the nature of the hysteresis is still under investigation and much scientific debate. The latter is not needed, since we can fit the ASA IV curves accurately and adding more parameters could lead to overfitting for these optimized high efficiency cells.

3. Case Study

The equations described in the previous section can be used to analyze the losses in a PV system. A PV system has been designed, based on a perovskite/silicon tandem cell. The performance of this system will be simulated at STC and for four different climate conditions.

3.1. The Design of the PV System

The reference cell that is used as a basis for the PV system is the monolithic perovskite/silicon two-terminal tandem designed at HZB by Al-Ashouri,[30] with a cell efficiency of 29.15%.

The structure of the cell is implemented in the Toolbox,[10] such that it can be used for simulations. The implementation in the Toolbox is both optical and electrical validated, as described by Vogt et al.[10] For the optical validation, the mean absolute deviation between measured and simulated EQE is only 1%. Also, the simulated photo current densities are within $0.1\,\text{mA}\,\text{cm}^{-2}$ of the measured short circuit densities. For the electrical validation, the mean absolute deviation between the measured and simulated IV curve is below $0.3\,\text{mA}\,\text{cm}^{-2}$ corresponding to 1.6%.

For the PV system in the simulation, encapsulation is added to the cells, which makes the modules more realistic.[10]

Additionally, the Si thickness is reduced from 260 to 160 μm to simulate a realistic value for an industrial solar cell, and the perovskite thickness is adjusted to achieve current matching under STC. The cell structure is shown in **Figure 3**. The EQE of the adjusted cell is also presented in this figure. The module consists of 72 cells, which are connected in series. Finally, the PV system consists of five modules in series, connected to an inverter. The same inverter is used for every location.

3.2. The Different Operating Conditions

The PV system is simulated under five different conditions, which includes STC and four different climates according to the Köppen–Geiger-photovoltaic (KGPV) classification.[31,32] The selected climates are temperate low irradiance climate (DL), the temperate high irradiance climate (DH), the tropical high irradiance (AH), and the temperate medium irradiance (DM). For each climate, a geographical location is selected, which are Amsterdam, Casablanca, Bombay, and Kyoto. The hourly climate data of each location are extracted from METEONORM version 7.3.[33] **Table 1** provides detailed information on the locations, such as the annual global horizontal irradiation (GHI), the mean annual ambient temperature (T_A), mean annual wind speed (WS), and the optimum fixed tilt for each location. For all locations, it is assumed that the horizon is free, and the modules are placed 1 and 8 m apart in the side spacing and row spacing, respectively.

3.3. Solar Tracking

For each location, three different solar tracking methods are simulated as well. Solar tracking is expected to increase the energy yield of a PV system as it increases the in-plane irradiance.[34] The different types of solar tracking are single axis (azimuth or altitude tracking) and double axis (simultaneous azimuth and altitude tracking). For azimuth only tracking, the tilt of the module is fixed, and the module's azimuth can move freely. For each
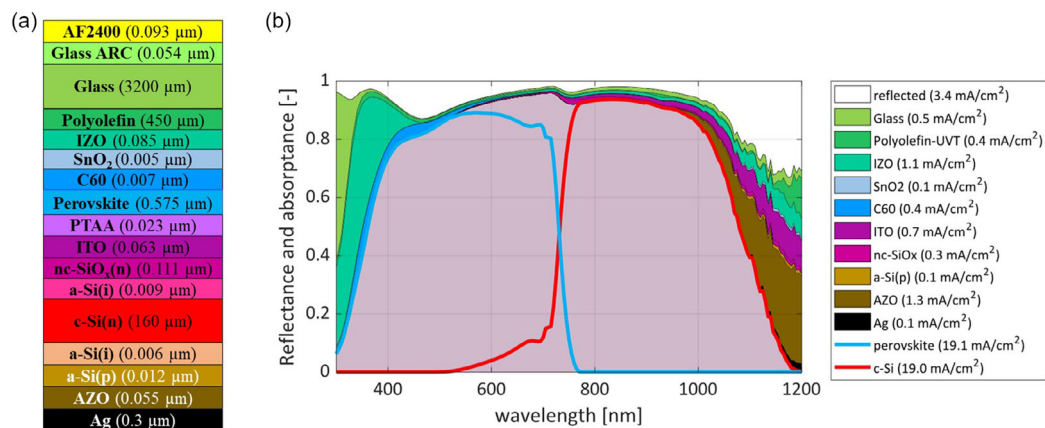
Figure 3. a) The encapsulated cell structure of the cell that is integrated into a module. For each layer, the thickness is indicated between brackets. b) The simulated EQE of the top and bottom cells. The absorbed photo-generated current in each layer is also presented.

Table 1. An overview of the different locations selected for the simulation.

| Location	Annual GHI [kWh m^{-2}]	Mean annual T_A [°C]	Mean annual WS [m s^{-1}]	KGPV	Optimum tilt [°]
Amsterdam (the Netherlands)	973	11.3	3.8	DL	32
Casablanca (Morocco)	1865	18.4	2.2	DH	26
Bombay (India)	1831	27.6	2.6	AH	19
Kyoto (Japan)	1286	16.2	1.8	DM	24

hour of the year, the azimuth that maximizes the incoming irradiance is chosen.

For altitude tracking, the module can rotate around the horizontal axis, whereas its azimuth is fixed. The tilt of the module is selected such that the incoming irradiance is maximized.

For azimuth and altitude combined tracking, the module will completely track the sun. This is simulated by setting the azimuth and altitude of the module equal to the azimuth and altitude of the sun.

4. Results and Discussion

The losses of the tandem modules are calculated for all conditions. The geographical locations have been simulated for a whole year, providing an annual energy loss analysis. First, the loss distribution at STC is presented, followed by the results and a discussion on the loss distribution at outdoors conditions. Also, the effect of the spectral variations and different temperatures are explained. Finally, the effect of solar tracking is discussed.
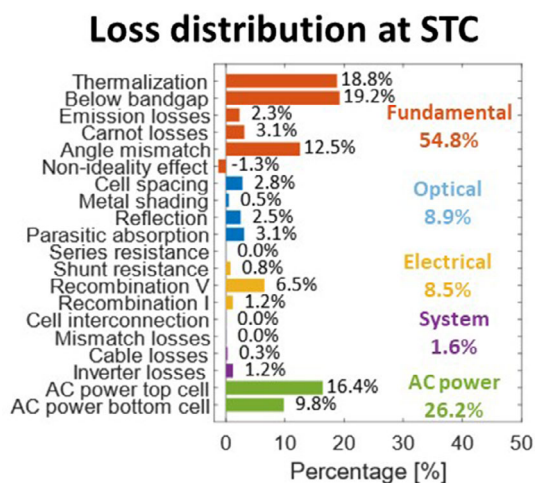
Figure 4. The loss distributions of the perovskite/silicon tandem at standard test conditions.

4.1. Results at Standard Test Conditions

The results at STC are presented in **Figure 4**. It can be seen that the AC efficiency is 26.2%. Each module (72 cells in series) has a short circuit of 4.63 A, an open circuit voltage of 121 V, a fill factor of 0.817, and an output power of 458 W. The area of a module is 1.80 m^2. The semiconductor module provides the temperature coefficient of the tandem modules. The temperature coefficient of the maximum power point and the open circuit voltage are around -0.21 and -0.18% K^{-1}, respectively. There is no temperature coefficient assumed for the short circuit current, as the photo-generated current is calculated before the thermal model.

The largest losses can be found in the fundamental losses, which have the same distribution as the integration over Figure 2. However, the fundamental losses are reduced by 1.3% once these nonideal cells are considered, which is mainly caused by a reduction in emission. More information on how the nonideality factor is built up can be found in the supporting information. Because the optimal voltage is higher than the actual voltage, the emission of an ideal cell is larger than the emission of a nonideal cell (as shown in Equation (3)).

The parasitic loses, in total 3.1%, are mostly caused by the IZO layer, accounting for 33% of the parasitic absorption. The electrical losses (8.5%) are for 62% caused by the perovskite cell and for 38% by the silicon cell.

4.2. The Loss Distribution under Outdoor Conditions

The difference between the loss distributions at STC and the real-world operating conditions is shown in **Figure 5**. The loss components are accumulated over one full year of simulation of the tandem PV system in the climate with hourly resolution. The annual efficiency (η_{year}) is calculated by summing the AC energy for each hour and dividing it by the total annual irradiation, which is written as

$$\eta_{\text{year}} = \frac{\sum_{t \in T} E_{\text{AC},t}}{\sum_{t \in T} E_{\text{in},t}} \qquad (20)$$

The value for each loss component is calculated in a similar method, where the summation of the hourly loss values is divided by the total incoming irradiation.

The PV system has the highest yearly efficiency in Casablanca (24.8%), and the other locations have an equal efficiency (24.0%). This is a decrease compared to the efficiency at STC (26.2%), which is mainly caused by the spectral variations and temperature differences.

The differences in loss distributions are caused by several phenomena. The spectral losses (thermalization and below bandgap losses) change due to a blue shift of the spectrum compared to AM1.5g. The blue shift is caused by the irradiance weighted air mass being lower compared at all simulated locations compared to STC. This causes an increase in the thermalization losses, but a decrease in below bandgap losses. Bombay has the lowest air mass, explaining why the difference compared to STC is the largest for this location.

The Carnot and angle mismatch losses increase at outdoors conditions. Due to a lower in-plane irradiance, the optimal
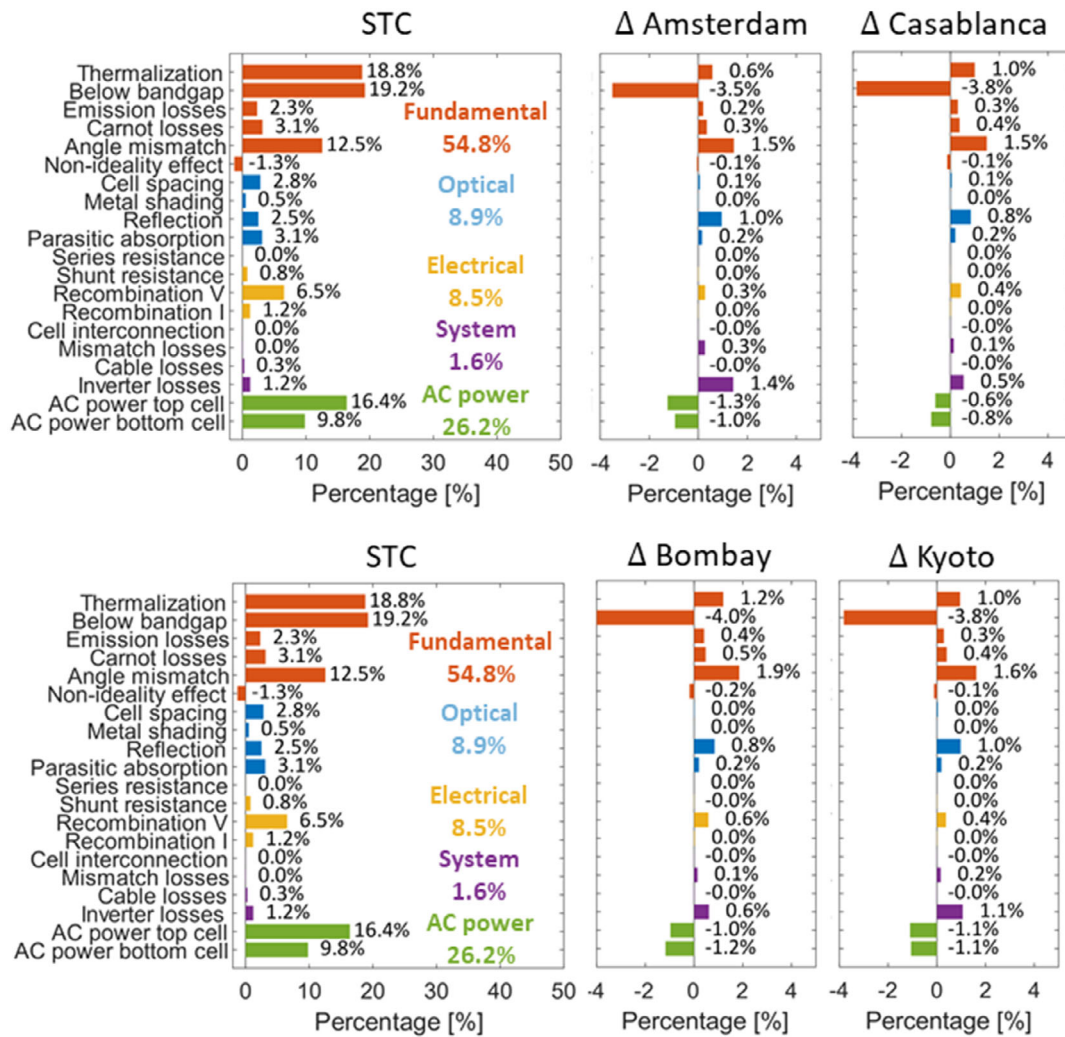
Figure 5. The difference between the loss distributions at STC and real-world operating conditions.

voltage decreases compared to STC. Since the Carnot and angle mismatch voltage account for the difference between the optimal voltage and $\frac{E_g}{q}$, these voltages increase. This leads to an increase of the Carnot and angle mismatch losses.

The reflection losses increase by 0.9%–1.0% (from 2.5% to 3.4%–3.5%), due to more oblique angles of incidence. An outdoor module receives light from multiple angles, which is different than at standard test conditions. This leads to more reflection.

Additionally, the inverter losses also increase significantly. Because the modules receive less irradiance compared to STC, the output power decreases. The selected inverter becomes less efficient at a lower power, resulting in more inverter losses. This also explains why the inverter losses are the largest in Amsterdam, since this location has the lowest in-plane irradiance.

The mismatch losses increase slightly due to spectral variations, resulting in a current mismatch. However, the current mismatch is largely compensated by the fill factor gain.[35] The fill factor gain is the phenomenon that the fill factor

increases, when the IV curves of the top and bottom cells are mismatched. An illustrative explanation of the fill factor gain is provided in the supplementary material. A quantification of the current mismatch, power mismatch, and fill factor gain is given in **Table 2**. The current mismatch is defined as $\frac{|I_{ph,top} - I_{ph,bot}|}{I_{ph,bot}}$, and the power mismatch is defined as $\frac{|P_{4T} - P_{2T}|}{P_{2T}}$, where P_{4T} is the output power if the cells would operate as four terminal. All values in the table are irradiance weighted over the whole year. The table shows that although the absorbed current mismatches are approximately 6%–7%, the mismatch in power is

Table 2. A quantification of the fill factor gain. The values shown are irradiance weighted over the full year.

	Amsterdam	Casablanca	Bombay	Kyoto	STC
Current mismatch [%]	7.03	6.16	7.02	6.43	0.18
Fill factor [–]	0.823	0.829	0.831	0.828	0.817
Power mismatch [%]	1.24	0.75	0.78	0.83	0.20

ADVANCED
SCIENCE NEWS
www.advancedsciencenews.com

Solar
RRL
www.solar-rrl.com
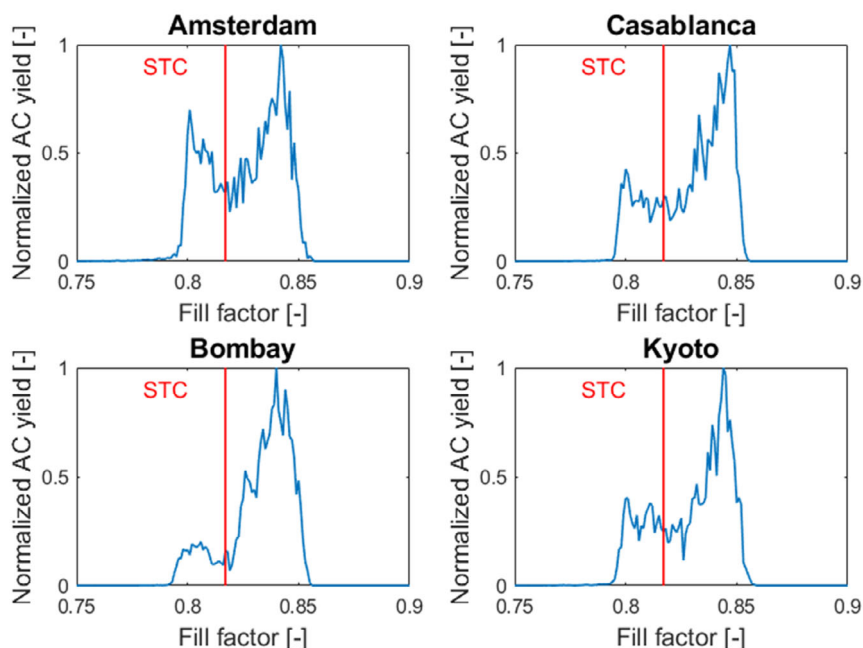
Figure 6. The relative AC energy yield for each fill factor. The red line indicates the fill factor at STC. It shows that at each location, most of the AC electricity is generated at a higher fill factor than the fill factor at STC.

only approximately 0.8%–1.2% as a result of higher fill factor. Note that the mismatch loss in Table 2 is relative to the incoming power, while the mismatch here is relative to the module power. **Figure 6** shows the normalized AC yield for different fill factors. The fill factor is discretized into steps of 0.1%, and the AC electricity generated in each step is added. Finally, the distribution is normalized according to the maximum value to obtain the plots shown in the figure. It can be seen that most of the energy yield is generated at a fill factor larger than at STC. This shows that the mismatch in implied photocurrent only is not a good indicator for estimating the mismatch losses. To correctly estimate the mismatch losses, power mismatch should be used.

### 4.3. The Comparison between Tandem and Single Junction Modules

The performance of the single junction modules has also been simulated to analyze the gain of combining the separate cells in a tandem. For the single junction modules, the top and bottom cells of the tandem cell (in Figure 3) are simulated separately.

The efficiencies at different operating conditions for the single and the tandem junction module are shown in **Table 3**. In the first rows, the AC efficiencies of the modules based on the top and bottom cells are reported for the different operating conditions. Also, the difference with the efficiency of the tandem cell is reported. On the third row, the efficiencies of the optimized c-Si modules are reported, including the difference with the tandem module. On the last row, the efficiencies of the tandem module under different conditions are shown. The absolute efficiency gain of using a tandem module is more than 5% compared to the optimized c-Si module for all locations. It should be noted that the efficiencies are AC system efficiencies, explaining why the values are lower than typical cell efficiencies mentioned in literature.

The most important reason for this gain is the reduction of thermalization/below bandgap losses for tandem modules. The c-Si PV systems perform the best in Casablanca, as this location has the highest incoming irradiation with a relative low temperature (see Table 1). The perovskite PV system (with a high bandgap energy) has the highest efficiency in Bombay, as this location has the lowest latitude and therefore the highest

Table 3. A comparison between the efficiency of the tandem and the single junction module at different operating conditions. The difference between the perovskite/silicon module is indicated between brackets.

Module	STC	Amsterdam	Casablanca	Bombay	Kyoto
η c-Si module based on bottom cell [%]	19.9 ($\Delta = 6.3$)	18.6 ($\Delta = 5.4$)	18.8 ($\Delta = 6.0$)	18.1 ($\Delta = 5.9$)	18.4 ($\Delta = 5.6$)
η perovskite module based on top cell [%]	19.3 ($\Delta = 6.9$)	16.6 ($\Delta = 7.4$)	17.5 ($\Delta = 7.3$)	17.1 ($\Delta = 6.9$)	16.8 ($\Delta = 7.2$)
η perovskite/silicon module [%]	26.2	24.0	24.8	24.0	24.0
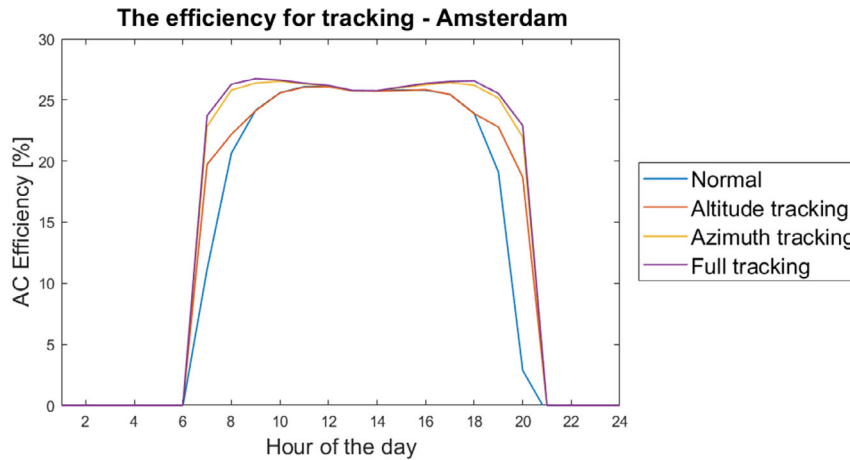
Figure 7. The efficiency of different tracking systems over different hours of 1 August. It can be seen that the efficiency increases especially in the morning and evening.

blue shift. The full loss distribution of the PV systems with single junction modules can be found in the supporting information.

4.4. The Effect of Solar Tracking

Solar tracking has an effect on the in-plane irradiation and on the efficiency of the tandem module. **Figure 7** shows how the efficiency of the different tracking systems changes over a certain day in Amsterdam. As example, 1 August is chosen, as this day has the highest efficiency. It can be seen that the efficiency increases especially in the morning and evening. This effect is the lowest for altitude tracking, as this method is not able to face the sun in the morning and evening as effective as the other methods. This is because the sun is typically in the east (morning) or in the west (evening) at these moments, while the module is facing south.

Table 4 shows the incoming irradiation, efficiency, and AC energy yield for the different types of tracking. The loss distribution for every simulation is presented in the supporting information. In the table, it can be seen that full tracking has the most effect regarding the in-plane irradiance, followed by azimuth tracking, and altitude tracking shows the least increase. Altitude tracking shows the least increase, since it cannot receive as much irradiance in the morning and evening as the other methods.

As shown in the table, the efficiency of a PV system can be affected by solar tracking. Full tracking has the largest effect and increases the efficiency in Amsterdam with 1.1% (from 24.0% to 25.1%). The efficiencies change due to lower angle mismatch, reflection, and inverter losses.

The angle mismatch losses, combined with the Carnot losses, are caused by the difference between the optimal voltage and the voltage corresponding to the bandgap energy. As the received irradiance increases with tracking, the optimal voltage also increases. This is because a greater irradiance allows the optimal voltage to be larger. As the optimal voltage increases, the difference between the optimal voltage and the bandgap voltage will

Table 4. The effect of solar tracking. It can be seen that solar tracking increases the incoming irradiance and can also increase the efficiency, leading to a higher energy yield.

Location	Type of tracking	Incoming annual irradiation [MWh]	Efficiency [%]	AC energy yield [MWh]
Amsterdam	None (Tilt = 32°)	10.2	24.0	2.45
	Azimuth tracking	12.3	24.9	3.06
	Altitude tracking	10.9	24.3	2.66
	Tracking both	13.2	25.1	3.32
Casablanca	None (Tilt = 26°)	18.8	24.8	4.67
	Azimuth tracking	22.5	25.4	5.72
	Altitude tracking	20.1	25.0	5.03
	Tracking both	25.0	25.7	6.41
Bombay	None (Tilt = 19°)	17.5	24.0	4.20
	Azimuth tracking	19.7	24.6	4.83
	Altitude tracking	18.4	24.3	4.46
	Tracking both	21.8	24.9	5.43
Kyoto	None (Tilt = 24°)	12.7	24.0	3.05
	Azimuth tracking	14.4	24.6	3.54
	Altitude tracking	13.5	24.3	3.28
	Tracking both	15.6	25.0	3.89

decrease, leading to a lower angle mismatch voltage. This leads to a decrease of angle mismatch losses.

When the PV modules tracks the sun, the angle of incidence will decrease for most of the incoming photons. The reflection is typically lower for small values of the angle of incidence. This decreases the reflection losses.

As mentioned before, the efficiency of the inverter typically increases for a greater output power. Because solar tracking increases the received irradiance, the output power will increase, leading to a higher inverter efficiency. Therefore, the inverter losses will decrease when tracking.

However, the mismatch losses increase when solar tracking is used. The absorption of the top and bottom cells is dependent on the angle of incidence and the spectral irradiance. Due to solar tracking, both of these parameters are changed. This leads to a different distribution of the absorbed current in the top and bottom cells. Eventually, this leads to more mismatch losses for all locations. Nevertheless, the efficiency increases for each type of tracking on each location.

The temperature of the PV modules will increase due to the larger incoming irradiance. For all locations, the increase of the temperature is on average smaller than 1 K. As the temperature coefficient of the PV module is around $-0.2\% \, \text{K}^{-1}$ (which is an output of the semiconductor module of the Toolbox, which uses the semiconductor device simulator ASA). Consequently, the efficiency is reduced by about 0.2% due to self-heating. However, this effect is smaller than the efficiency increasing effects described earlier.

Due to the increase on the in-plane irradiation and the effect on the efficiency, the AC energy yield increases for tracking. Similar to the in-plane irradiation, the effect is the largest for full tracking, followed by azimuth tracking.

5. Conclusion

In this work, a model for calculating the losses is presented. Totally, 17 losses are defined and divided into four categories. This model is applied on the simulation of a PV system, based on the perovskite/silicon tandem cell fabricated by HZB.[30] This PV system is simulated at STC and at various climates. For each operating condition, the loss distributions are presented and compared among each other. It is also shown that the efficiency of tandem modules is significantly larger than single junction modules for all operating conditions. Finally, solar tracking is simulated to observe the effects on the loss distribution.

There were several differences in the loss distribution at STC and at the outdoor location. The thermalization and below bandgap losses changed significantly due to a blue shift of the spectrum. The blue shift is the highest in Bombay, since the sun is the highest at this location. Also, the reflection losses increased with 0.9%–1.1% due to more oblique angles of incidence.

Additionally, it was shown that solar tracking can increase the energy yield of a PV system due to two reasons. First, the in-plane irradiation of the system increases, as the module faces the sun. Second, the efficiency of a PV system increases by solar tracking. As reason for this efficiency increase, we identified that angle mismatch, reflection, and inverter losses decrease when the module follows the sun. However, the mismatch losses increase when solar tracking is used, as the increased in-plane irradiance at lower sun elevation results in a larger current and power mismatch.

Finally, we quantified that mismatch losses due to changes in the spectrum are not as large as the current mismatch indicates. A difference in photo-generated current will lead to gain in fill factor (the fill factor gain), limiting the power loss. Due to the fill factor gain, a difference of 7.0% in absorbed current will only lead to a power mismatch of 1.2%. Therefore, the power mismatch should be used as indicator for mismatch losses instead of a current mismatch.

Supporting Information

Supporting Information is available from the Wiley Online Library or from the author.

Conflict of Interest

The authors declare no conflict of interest.

Data Availability Statement

The data that support the findings of this study are available from the corresponding author upon reasonable request.

[1] A. G. Aberle, W. Zhang, B. Hoex, *Energy Procedia* **2011**, *8*, 244.
[2] I. Haedrich, D. C. Jordan, M. Ernst, *Sol. Energy Mater. Sol. Cells* **2019**, *202*, 110069.
[3] S. Aragwal, P. R. Nair, *J. Appl. Phys.* **2018**, *124*, 183101.
[4] T. Ma, Z. Guo, L. Shen, X. Liu, Z. Chen, Y. Zhou, X. Zhang, *Appl. Energy* **2021**, *298*, 117205.
[5] I. M. Peters, Y. S. Khoo, T. M. Walsh, *IEEE J. Photovoltaics* **2014**, *4*, 585.
[6] A. Khanna, T. Mueller, R. A. Stangl, B. Hoex, P. K. Basu, A. G. Aberle, *IEEE J. Photovoltaics* **2013**, *3*, 1170.
[7] L. Shen, Z. Li, T. Ma, *Appl. Energy* **2020**, *260*, 114333.
[8] A. Wang, Y. Xuan, *Energy* **2018**, *144*, 490.
[9] H. Liu, C. D. Rodríguez-Gallegos, Z. Liu, T. Buonassisi, T. Reindl, I. M. Peters, *Cell Rep. Phys. Sci.* **2020**, *1*, 100037.
[10] M. R. Vogt, C. Ruiz Tobon, A. Alcañiz, P. Procel, Y. Blom, A. Nour El Din, T. Stark, Z. Wang, E. Garcia Goma, J. G. Etxebarria, H. Ziar, M. Zeman, R. Santbergen, O. Isabella, *Sol. Energy Mater. Sol. Cells* **2022**, *247*, 111944.
[11] C. A. Gueymard, *Sol. Energy* **2019**, *187*, 233.
[12] R. Perez, R. Seals, J. Michalsky, *Sol. Energy* **1993**, *50*, 235.
[13] M. K. Fuentes, SAND-85-0330, **1987**.
[14] W. Shockley, H. J. Queisser, *J. Appl. Phys.* **1961**, *32*, 510.
[15] L. C. Hirst, N. J. Elkins-Daukes, *Prog. Photovoltaics: Res. Appl.* **2011**, *19*, 286.
[16] W. Ruppel, P. Wurfel, *IEEE Trans. Electron Devices* **1980**, *27*, 877.
[17] M. A. Alam, M. R. Khan, *Appl. Phys. Lett.* **2016**, *109*, 173504.
[18] M. A. Alam, M. R. Khan, *Proc. Natl. Acad. Sci.* **2019**, *116*, 23966.
[19] M. Ryyan Khan, M. A. Alam, *Appl. Phys. Lett.* **2015**, *107*, 235502.
[20] A. De Vos, *J. Phys. D: App. Phys* **1980**, *13*, 839.
[21] F. Urbach, *Phys. Rev.* **1953**, *92*, 1324.
[22] J. D. Dow, D. Redfield, *Phys. Rev. B* **1972**, *5*, 594.
[23] M. Zeman, J. Van Den Heuvel, M. Kroon, J. Willeman, B. Pieters, J. Krč, S. Solntsev, **2019**, Technical report 8.
[24] T. Ma, H. Yang, L. Lu, *Sol. Energy* **2014**, *100*, 31.

[25] A. Chouder, S. Silvestre, B. Taghezouit, E. Karatepe, *Sol. Energy* **2013**, *91*, 337.

[26] K. Ramalingam, C. Indulkar, in *Distributed Generation Systems*, Elsevier, Amsterdam **2017**, pp. 69–147.

[27] W. Bludau, A. Onton, W. Heinke, *J. Appl. Phys.* **1974**, *45*, 1846.

[28] T. Dittrich, C. Awino, P. Prajongtat, B. Rech, M. C. Lux-Steiner, *J. Phys. Chem. C* **2015**, *119*, 23968.

[29] W. Raja, M. De Bastiani, T. G. Allen, E. Aydin, A. Razzaq, A. U. Rehman, E. Ugur, A. Babayigit, A. S. Subbiah, F. H. Isikgor, S. De Wolf, *Nonophotonics*, **2021**, *10*, 2023.

[30] A. Al-Ashouri, E. Köhnen, B. Li, A. Magomedov, H. Hempel, P. Caprioglio, J. A. Márquez, A. B. Morales Vilches, E. Kasparavicius, J. A. Smith, N. Phung, D. Menzel, M. Grischek, L. Kegelmann, D. Skroblin, C. Gollwitzer, T. Malinauskas, M. Jošt, G. Matič, B. Rech, R. Schlatmann, M. Topič, L. Korte, A. Abate, B. Stannowski, D. Neher, M. Stolterfoht, T. Unold, V. Getautis, S. Albrecht, *Science* **2020**, *370*, 1300.

[31] J. Ascenio-Vásquez, K. Brecl, M. Topič, *Sol. Energy* **2019**, *191*, 672.

[32] M. C. Peel, B. L. Finlayson, T. A. McMahon, *Hydrol. Earth Syst. Sci.* **2007**, *11*, 1633.

[33] J. Remund, S. Müller, M. Schmutz, P. Graf, Meteonorm Software, **2020**.

[34] M. Babics, M. De Bastiani, A. H. Balawi, E. Ugur, E. Aydin, A. S. Subbiah, J. Liu, L. Xu, R. Azmi, T. G. Allen, A. U. Rehman, T. Altmann, M. F. Salvador, S. De Wolf, *ACS Energy Lett.* **2022**, *7*, 1604.

[35] C. Battaglia, J. Escarré, K. Söderström, L. Erni, L. Ding, G. Bugnon, A. Billet, M. Boccard, L. Barraud, S. De Wolf, F. Haug, M. Despeisse, C. Ballif, *Nano Lett.* **2011**, *11*, 661.